Effect of corrosion pit on fatigue damage and failure in powder bed fusion AlSi10Mg

Effect of corrosion pit on fatigue damage and failure in powder bed fusion AlSi10Mg

Haipeng Song[a,*], Rubi Liang[a], Sheng Jiang[a], Hao Zhang[b], Juan Du[a], Dinghe Li[a], Qian Zhang[c], Sean B. Leen[d,e,f]

[a] *Sino-European Institute of Aviation Engineering, Civil Aviation University of China, China*

[b] *College of Mechanical Engineering, Yangzhou University, China*

[c] *Tianjin Key Laboratory of Modern Engineering Mechanics, School of Mechanical Engineering, Tianjin University, China*

[d] *School of Engineering, College of Science and Engineering, University of Galway, Ireland*

[e] *Ryan Institute, University of Galway, Ireland*

[f] *I-Form Advanced Manufacturing Research Centre, Ireland*

Abstract

This paper is concerned with environmental corrosion during service of load-bearing aluminum alloys fabricated by additive manufacturing (AM) with a focus on damage evolution characterisation and identification of dominated failure mechanisms of pre-corroded selective laser melted aluminum alloy. An experimental strategy for analysis of the damage and failure process is presented, combining 3D surface measurement, 3D digital image correlation and scanning electron microscopy, to provide multi-source experimental characterization of corrosion morphology, strain field evolution and fracture morphology. Statistics and machine learning methods were employed to process the measured multi-source experimental data, showing that local average roughness has a strong influence on macro-crack initiation position. The analysis focuses on four primary types of fatigue micro-crack initiation, namely internal defects, corrosion platform, corrosion micro-pit and corrosion jut-in; internal defects and corrosion platform are unique features for powder bed fusion (PBF) AlSi10Mg. The micro-crack initiation mechanisms for all four types are (i) local stress concentrations due to adjacent material micro-structural defects, (ii) interaction of underlying alloy microstructure and corrosion-induced stress/strain, and (iii) local stress/strain concentration at corrosion micro-pit and jut-in, respectively.

Keywords: Digital image correlation; Additive manufacturing; Corrosion pit; Damage evolution; Failure mechanism

---

* Corresponding author.

E-mail address: hpsong@cauc.edu.cn (Haipeng Song)

Nomenclature

AA	Aluminum alloys
AM	Additive manufacturing
A and B	Material constants
D_f	Damage severity factor
DIC	Digital image correlation
EXCO	Exfoliation corrosion
$k_{t\text{-}e}$	Elastic stress concentration factor
k_{ε}	Strain concentration factor
LOF	Lack of fusion
m	Points exhibiting high strain levels
N	Total number of points within the analysis region
N_f	Number of cycle at failure
OM	Optical microscopy
R	Stress ratio
RMS	Root mean square
S	Stress amplitude
SEM	Scanning electron microscope
PBF	powder bed fusion
3D-DIC	Three-dimensional digital image correlation
α and β	Model fitting parameters
σ_m	Peak stresses
$\overline{\varepsilon}$	Average strain
$\bar{\varepsilon}_{max}$	Maximum value of $\overline{\varepsilon}$
$(\varepsilon_{eq})_i$	Von Mises strain at measured point i

1. Introduction

Additive manufacturing (AM) technology is suitable for the manufacture of advanced lightweight industrial components with flexible geometric configurations and intricate internal architectures[1]. As a particular rapid prototyping AM technique, powder bed fusion (PBF) uses a high-energy-density laser beam to scan the fully molten metal powder and resolidifies the molten pool to achieve the effect of metallurgical bonding[2,3], which is now widely used in the fabrication of advanced alloys, such as titanium alloys and aluminum alloys (AA)[4,5]. With the increasing requirements for lightweight, energy saving and emission reduction, high-performance AM aluminum alloys is becoming a current research hotspot, due to its low density and excellent processability. AM aluminum alloys not bear load but also suffer from environmental corrosion during service; thus it is important to conduct research on damage and failure of AM aluminum alloys considering both corrosion and loading conditions.

There is significant recent interest in the corrosion behavior of AM aluminum alloys. PBF AlSi10Mg has been shown to have significantly better corrosion resistance than most traditional casting aluminum alloys[6]. Based on electrochemical tests, Bi *et al.* illustrated that AM Al14.1Mg0.47Si0.31Sc0.17Zr alloy has higher polarizability and better electrode reaction resistance than conventional aluminum alloy[7]. The corrosion behavior of PBF Al-Si alloys has been shown to relate closely to microstructure[8,9]. Torbati-Sarra *et al.* analyzed AM Al-6061 alloy corrosion behavior exposed to 0.5M NaCl solution by electrochemical measurement and microscopy observation, and showed that titanium-rich and B_4C particles in the AM matrix reduce oxide layer integrity, resulting in barrier film cracking and severe localized corrosion[9]. Zhang *et al.* studied the relationship between corrosion behavior and material microstructure in AM AA2024 alloy, showing that melt pool border is more susceptible to localized corrosion than melt pool zone and heat affected zone, due to the relatively high volume fraction of eutectic S-phase resulting from alloying element segregation during solidification[10].

Material post-processing treatment, e.g. heat treatment and surface treatment, also affect AM material corrosion performance[11-15]. By analyzing the potentiodynamic polarization data of PBF AlSi10Mg in NaCl solution, Leon *et al.* revealed that polished samples exhibited lower surface corrosion potential compared to unpolished, indicating correlation between corrosion resistance and surface roughness for AM aluminum alloy[14]. Wei *et al.* studied the microstructure evolution of PBF AlSi10Mg at different T6 heat treatment temperatures and the corrosion behavior in an acidic environment. The results demonstrated that pristine samples exhibit a selective corrosion attack at molten pool boundaries, whereas the T6 heat-treated samples show pitting corrosion and pit growth with increasing solution temperature[16]. Rubben *et al.* investigated effect of heat treatment on microstructure and corrosion behavior of AM AlSi10Mg, showing that morphology of corrosion is related to silicon morphology affected by heat treatment[17].

Loading-induced damage and failure of AM aluminum alloys have also received wide attention, especially for fatigue performance. A number of authors have confirmed that internal defects are important to fatigue life of AM aluminum alloys[18-20]. A strength altering factor is proposed to extrapolate fatigue curves for AM specimens containing different defects, indicating that fatigue curves of specimens with different initial defect sizes are closely related[21]. Ferro *et al.* studied the fatigue process of AlSi10Mg fabricated by laser PBF through scanning electron microscope (SEM) fractography, and found that most fatigue cracks originate at large and irregular unmelted surface defects, whereas fewer nucleate at well-distributed and regular-shaped pore defects[22].

For the evaluation of the relationship between internal defects and fatigue, Niu *et al.* applied extreme value statistics and weakest-link theory to the evaluation of defect tolerance fatigue under size effect, and established a probabilistic framework to effectively estimate the fatigue strength/life of AM materials[23]. Wang *et al.* developed a defect-driven physically informative neural network (PINN) to assess the influence of defect features on fatigue performance and scatter of AM materials, showing good accuracy in fatigue life prediction[24].

The fatigue performance of AM aluminum alloys is inseparable from manufacturing process parameters, which typically determine material microstructure and internal defects of final product, thereby affecting fatigue failure behavior[3,25-27]. Wang *et al*. conducted in-situ SEM fatigue tests on PBF AlSi10Mg under different scanning speeds and laser energies, and demonstrated a strong correlation between porosity and fatigue resistance; higher scanning speed can help to reduce porosity[28]. Larossa *et al.* discovered that the fatigue life of AM aluminum alloy specimens perpendicular to the build direction exceeded those tested parallel to it[29]. Wu *et al.* investigated the effect of defect population on the anisotropic fatigue resistance of AM AlSi10Mg; large oblate (pancake-shaped) defects were found to orient primarily within the build plane leading to a highly anisotropic fatigue strength[30]. Jian *et al.* studied the high-cycle fatigue behavior of PBF AlSi10Mg with different printing powder sizes, and showed that samples with small powder sizes have high defect content and low fatigue life[31]. In addition, numerous studies report that appropriate heat treatment can improve AM AlSi10Mg components' fatigue strength, attributed to the improvement of material structure homogenization[32-34]. Aboulkhair *et al.* illustrated that heat treatment can induce microstructural transformation, reduce residual stress, and prolong fatigue life for PBF AlSi10Mg[35]. To sum up, relationships between fabrication procedure, mechanisms involved in internal defect formation, control of post-processing residual stress, and fatigue performance of AM AlSi10Mg alloys has previously been explored.

So far, research efforts have primarily concentrated on investigating the separate characteristics of corrosion behavior and failure mechanisms in AM aluminum alloys; only a few researchers have investigated damage and failure of materials under pre-corrosion fatigue or corrosion-fatigue conditions. Combining corrosion fatigue tests and SEM fracture analysis, Leon *et al.* found that numerous pores and other defects on the PBF aluminum alloy surface, which causes local pitting corrosion, leading to crack initiation and propagation[14]. However, comprehensive experimental analysis considering cross-scale behaviour (e.g. combined macro-micro fracture behavior) and temporal-spatial characteristics (e.g. full-field, full-process observation) of damage evolution in pre-corroded AM aluminum alloys is still lacking, especially associated with the diverse corrosion morphology;

some key problems, such as the influence of local corrosion morphology on macro-crack formation, dominant forms of micro-crack initiation and the corresponding intrinsic failure mechanisms, remain unclear.

To this end, experimental investigations were conducted here on pre-corroded PBF AlSi10Mg damage evolution and failure mechanisms under uniaxial fatigue loading. Due to the interaction between multiple corrosion pits, the crack initiation and propagation behavior can be affected[36,37]. In order to evaluate the individual behavior of cracks originating from a single pit under fatigue loading, an artificial isolated corrosion pit was designed into the specimens. An experimental strategy combining 3D surface measurement, 3D digital image correlation (3D-DIC) and SEM was implemented, to provide multi-source experimental information concerning corrosion morphology, strain field evolution, and fracture morphology. Statistics and machine learning were employed to process the measured multi-source experimental data, evaluating the importance of typical corrosion morphology characteristic parameters on macro-crack initiation. Based on the experimental observations and statistical analysis, comprehensive discussion and analysis on the influence of corrosion pits on fatigue damage evolution and failure mechanisms in PBF aluminum alloy is presented.

The subsequent sections of the paper are as follows: Section 2 describes materials and specimens, corrosion pit preparation and fatigue test; Section 3 presents experimental results of fatigue life, 3D-DIC-based fatigue damage evolution and SEM-based fracture morphology; in Section 4, discussion on damage evolution and failure mechanism in pre-corroded AM aluminum alloy are given; finally, conclusions are drawn in Section 5.

2. Experiment

2.1. Material and specimen

The material PBF AlSi10Mg was manufactured by SimpNeed Co. Ltd, China. The specific composition is shown in Table 1. A fiber laser beam has been used in the 3D printing process to irradiate the matrix through a scanning mirror, melting the metal powder. As the powder quickly melts and solidifies, the base moves down to form one layer of components after scanning, and the powder is supplied by the powder pool, finally forming the desired part[38]. The samples were constructed along the L (90°) direction, and the relevant process parameters are shown in Table 2 (provided by the manufacturer SimpNeed Co. Ltd). Mechanical properties of the material were obtained by quasi-static uniaxial tension tests conducted under monotonic loading along the L direction at room temperature. The material exhibited an elastic modulus of 71.2 GPa, a yield strength of 267.4 MPa, a tensile strength of 474.2 MPa, and an elongation of 5.7%.

Table 1. PBF AlSi10Mg specimen composition (wt. %).

Element	Si	Cu	Mn	Mg	Fe	Ti	Ni	C	Al
SLM AlSi10Mg	9.0~10.0	≤0.05	≤0.45	0.2~0.45	≤0.55	≤0.15	≤0.05	≤0.0075	Bal.

Table 2. Process parameters recommended for PBF AlSi10Mg.

Layer thickness/μm	Laser power/w	Scan velocity/mm s^{-1}	Scanning spacing/mm	Platform temperature/°C	Powder Size/μm	Environment
35	350	1000	0.18	200	15-33	Ar

The microstructure of PBF AlSi10Mg was observed by optical microscopy (OM). After mechanical grinding to #2000 and polishing with a 1 μm diamond suspension, the sample surface was etched using Keller's reagent (2 mL HF, 3 mL HCl, 5 mL HNO_3, and 100 mL distillate). Using AxioLab A1 optical microscope (Zeiss, Germany) to analyze the sample surface metallography, as shown in Fig. 1. Since the cross section along the build direction consists of the melted zone, studying the structure of the melted zone resulting from the laser power Gaussian distribution is crucial. The powder located in the center of the laser beam absorbs a higher amount of energy compared to the powder situated at the edges. Consequently, complete melting occurs for some powder while other particles remain partially melted, giving rise to a distinct molten pool structure[38].

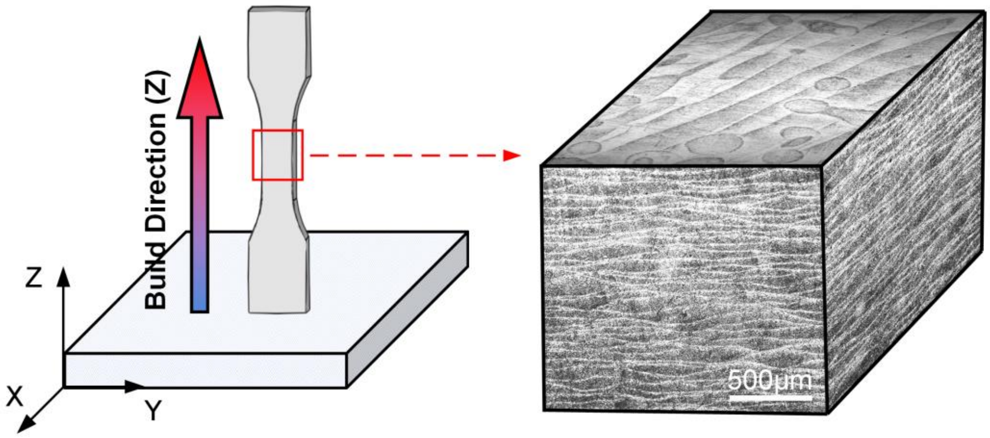

Fig. 1. Microstructure of PBF AlSi10Mg in three mutually perpendicular planes before testing.

2.2 Corrosion pit preparation

In order to study the effect of corrosion damage on the fatigue behavior, the electrochemical corrosion method was used to create an artificial corrosion pit on the specimen surface[39], as shown in Fig. 2 (a). Exfoliation corrosion (EXCO) solution was prepared according to ASTM G34-01[40]: sodium chloride (234 g NaCl), potassium nitrate (50 g KNO_3), nitric acid (6.3 mL HNO_3), and 1 L distilled water diluted. All pre-corroded specimens were obtained in the same way, with 12 h specific exposure time to fully achieve the central isolated corrosion pit. All samples were cleaned in an ultrasonic bath for 10 minutes, washed with ethanol, and dried after corrosion. Then IFM G5 optical surface measuring instrument (Alicona, Austria) was used to identify the 3D morphology and characteristic parameters of prepared corrosion pits. In preparation for the subsequent 3D-DIC analysis, a uniform distribution of random speckle was created on the surfaces of all samples by applying black and white spray.

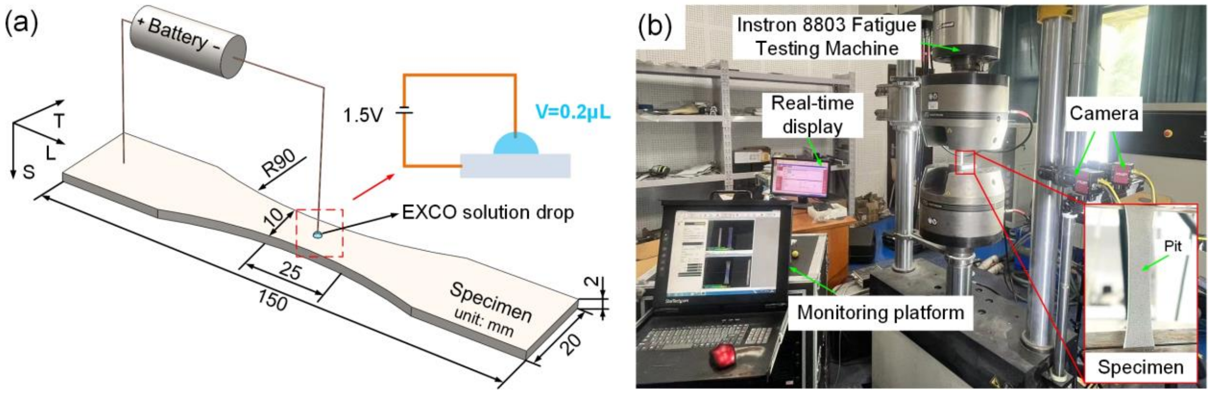

Fig. 2. (a) Schematic diagram of fatigue specimen size and pre-corrosion preparation; (b) experimental setup for uniaxial fatigue test.

2.3 Fatigue test and 3D digital image correlation

The original and pre-corroded PBF specimens were sequentially subjected to constant amplitude fatigue tests with different peak loads at room temperature, as shown in Fig. 2 (b). In all experiments, the control applied axial load adopted a sinusoidal waveform, with 5 Hz frequency and 0.1 stress ratio (R)[41]. The three different peak stresses σ_m were set as 214 MPa, 187 MPa, 160 MPa, which are 60%, 70%, and 80% of the material yield strength respectively. Each loading condition was repeated three times to ensure the reliability and consistency of the experiments.

During the fatigue process, the commercial software VIC-3D (Correlated Solutions, Inc., America) was used to capture the stereo images of specimen surface at specific cycles, with 1524 × 3205 pixels. Prior to the testing, the camera parameters were calibrated by using a standard calibration grid. After fatigue tests, the acquired images were analyzed using VIC-3D software, employing a size of 25 × 25 pixels and a step of 1 pixel. This allowed for the calculation of displacement and strain fields within the designated analysis areas, visualizing the spatial-temporal characteristics of macro-crack formation and propagation to failure. Furthermore, through the statistical analysis of DIC strain fields, damage severity curves were determined. Then S-3400N SEM (Hitachi, Japan) was used to characterize the fracture micro-morphology.

Particularly, for pre-corroded specimens, due to the small corrosion pit depth (within the depth of field), the central isolated corrosion pit with ellipsoid shape can be effectively identified by 3D-DIC, as shown in Fig. 3 (a), (b), which is basically consistent with the SEM fracture measurement result as shown in Fig. 3 (c). Thus, the 3D-DIC method is verified to be helpful to analyze the strain evolution in/around the pit. Based on the DIC strain fields, the damage severity factor was computed to measure the average deformation deviation and effectively assess the severity of specimen damage[42].

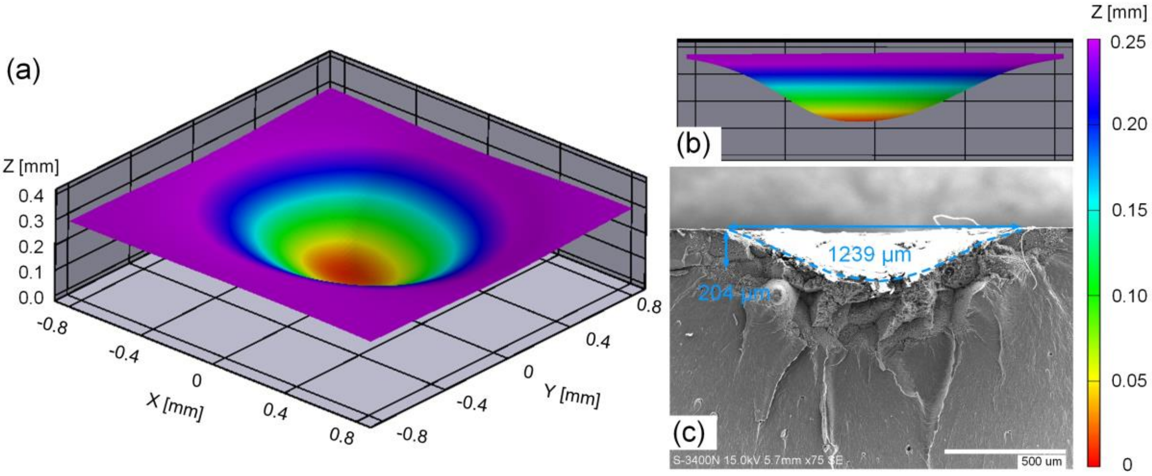

Fig. 3. 3D morphology of corrosion pit observed by DIC: (a) isometric view, (b) front view; (c) Corrosion pit morphology identified by SEM.

A damage severity factor D_f is defined, to quantify integrated damage for the complete specimen, based on the the DIC measured distribution of strain, as follows[42]:

$$D_f = \frac{\overline{\varepsilon}}{\overline{\varepsilon}_{\max}} \tag{1}$$

$$\bar{\varepsilon} = \left(\frac{1}{m}\sum_{i=1}^{m}(\varepsilon_{eq})_i - \frac{1}{N}\sum_{i=1}^{N}(\varepsilon_{eq})_i\right) \tag{2}$$

where $(\varepsilon_{eq})_i$ is the equivalent strain at measured point i, N represents the total number of points within the region of interest (~1000 here), and m indicates the count (~100 here) of specifically chosen measurement points exhibiting high strain levels (top 1% of the total number is selected here with reference to the literature[42]). To numerically assess damage severity, the discrepancy between the average strain of selected points and the overall average strain can be quantified as $\overline{\varepsilon}$. As fatigue damage accumulates, $\overline{\varepsilon}$ continues to increase and reaches a maximum value $\overline{\varepsilon}_{\max}$ at failure. D_f is thus defined at the normalised version of $\overline{\varepsilon}$.

3. Result

3.1. Fatigue life under different peak stresses

Fig. 4 and Table 3 show the peak stress-fatigue life results measured for un-corroded and pre-corroded PBF AlSi10Mg under different peak load. The fitting curves are also given in Fig. 3 based on the Basquin mode [43]:

$$S = A(N_f)^B \tag{3}$$

A simplified expression can be obtained as follows:

$$\sigma_{\max} = \alpha(N_f)^\beta \tag{4}$$

where S is the stress amplitude, A and B are material constants, N_f is the number of cycles at failure, σ_m is applied peak stress, α and β are model fitting parameters. The experimental results show that the mean life decreases progressively as the peak stress increases, while keeping the stress amplitude ratio constant. Corresponding to 160 MPa, 187 MPa and 214 MPa maximum stresses, the uncorroded average fatigue life results were 73,913, 41,621 and 26,036 cycles, respectively. The average lifespans of pre-corroded specimens were 28,057, 15,752 and 8,491 cycles, respectively, decreased by about 62.0%, 62.2% and 67.4% than original specimens. Pre-corrosion has been observed to significantly accelerate the fatigue failure process according to the experimental results, leading to significantly fatigue property degradation of PBF AlSi10Mg.

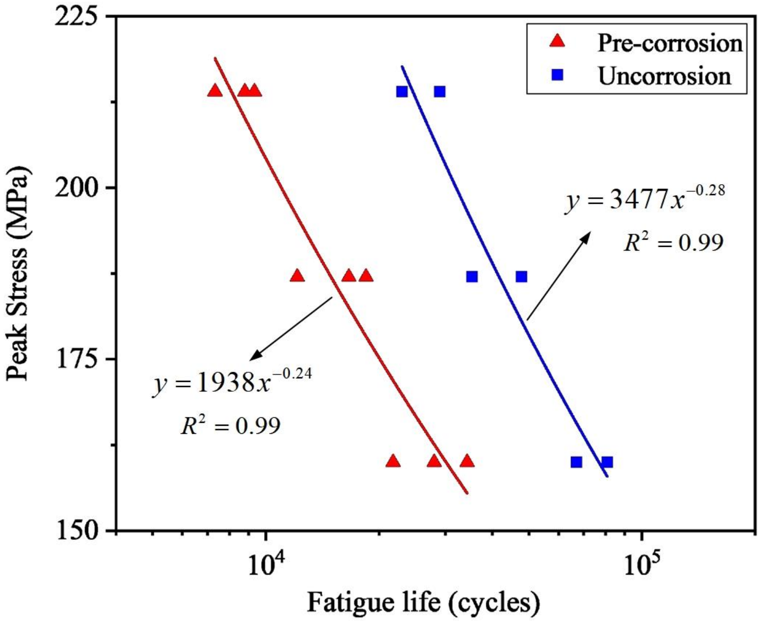

Fig. 4. Measured fatigue life of pre-corroded and uncorroded PBF AlSi10Mg under different peak stresses.

Table 3. Uniaxial fatigue test results of pre-corroded PBF AlSi10Mg under different peak stresses.

Peak Stress (MPa)	Specimen No.	Fatigue life (cycles)	Average life (cycles)	Macro-crack location identified by DIC	Location Schematic
	1-1	7,335		sidewall	
214	1-2	8,806	8,491	sidewall + mouth	
	1-3	9,332		sidewall	
	2-1	12,137		bottom + mouth	
187	2-2	16,629	15,752	bottom	
	2-3	18.488		sidewall	

	3-1	21,806		sidewall + mouth	
160	3-2	28,047	28,057	sidewall + mouth	
	3-3	34,317		sidewall + mouth	

3.2 Fatigue damage evolution by 3D-DIC

In order to describe the spatial-temporal characteristics of fatigue damage evolution, the equivalent strain fields of un-corroded and pre-corroded PBF AlSi10Mg specimens under different loading conditions were calculated by 3D-DIC. Typical damage severity curves of un-corroded pre-corroded and PBF AlSi10Mg subjected to uniaxial fatigue loading are also presented, revealing that failure involves three distinct stages: damage accumulation, macro-crack formation (the inflection point), and propagation. Fig. 5 shows the typical equivalent strain fields for original PBF AlSi10Mg at various peak stresses, together with the computed damage severity curves. No obvious localization damage was observed for σ_m = 214 MPa before 1.589 $\times 10^4$ cycles (A_1 in Fig. 5). When reaching 2.882 $\times 10^4$ cycles, a local strain concentration region I_1 appeared on the specimen left boundary (B_1 in Fig. 5, shown by the white arrow), which corresponds to point B_1 on the damage curve, indicating that fatigue damage accumulation led to macro-crack I_1 formation. After that, crack I_1 gradually expanded (C_1 in Fig. 5), and finally caused failure at 29,026 cycles (D_1 in Fig. 5). For σ_m=187 MPa, damage accumulation resulted in emergence of a local high strain region II_1 (B_2 in Fig. 5) on the upper right boundary at 4.717$\times 10^4$ cycles, forming macro-crack II_1, associated with inflection point B_2. With increasing cycles, macro-crack II_1 gradually propagated (C_2 in Fig. 5) and finally caused rapid complete fracture at 47,871 cycles (D_2 in Fig. 5). For σ_m=160 MPa, no local concentrated strain phenomenon was visible until 39,585 cycles (A_3 in Fig. 5). At 6.606 $\times 10^4$ cycles, matching the inflection point B_3 of the damage curve, region III_1 of strain concentration occurred on the lower left boundary, resulting in macro-crack formation. With increasing fatigue cycles, macro-crack III_1 continued to propagate (C_3 in Fig. 5), and eventually led to a fragmented fracture at 67,019 cycles (D_3 in Fig. 5).

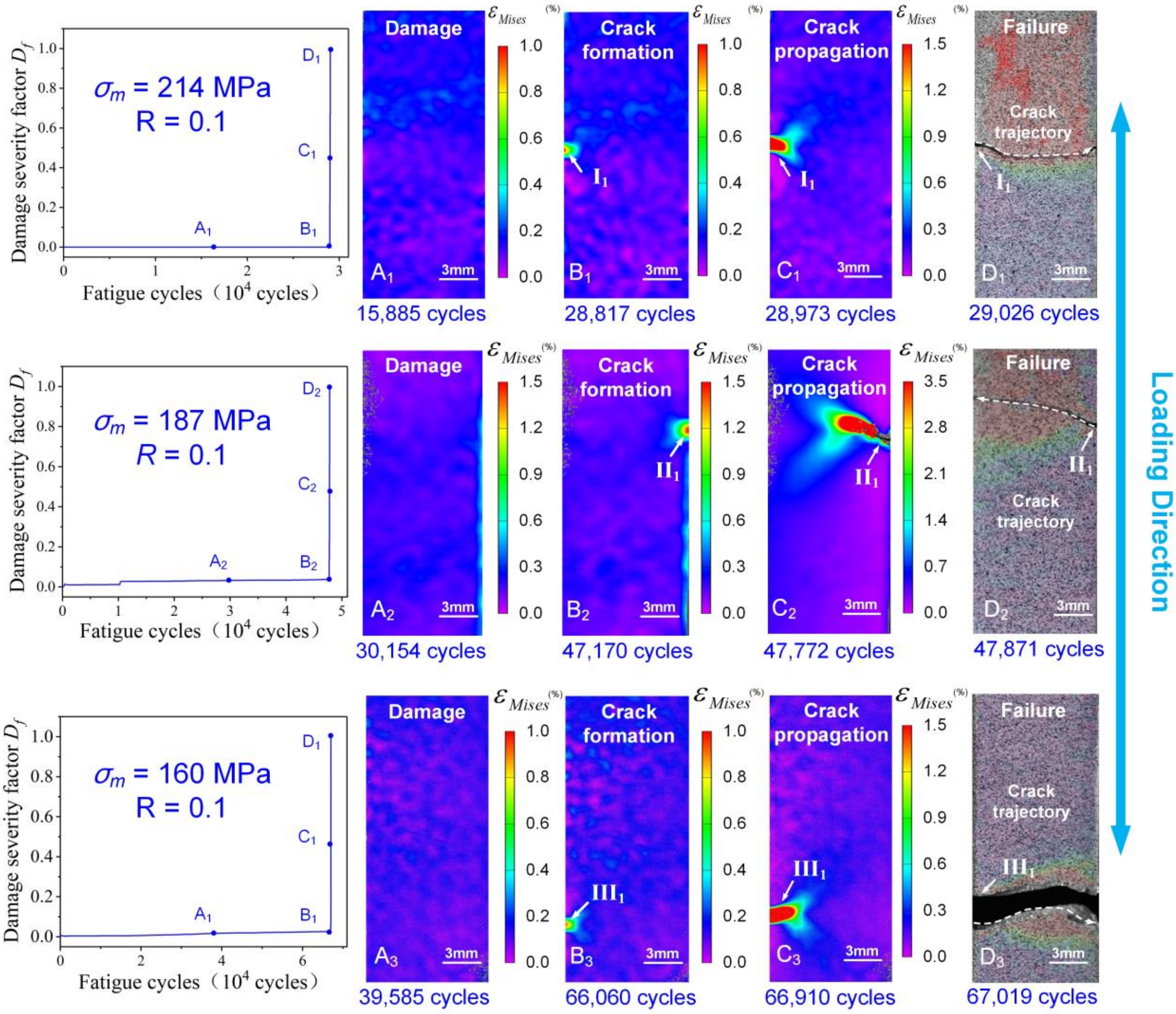

Fig. 5. Visualization of damage evolution, crack formation and propagation in original PBF AlSi10Mg specimens for different applied stress levels, represented by damage severity curves and equivalent strain fields shown in the colored images.

The progression of fatigue damage for pre-corroded PBF AlSi10Mg at different peak stresses can be deduced by examining the DIC strain maps and the damage severity curves depicted in Fig. 6. Isometric views of the strain fields for macro-crack formation are also given, clearly showing the specific location of crack nucleation sites at the corrosion pit. Compared with the un-corroded specimen, the center isolated pits formed by the pre-corrosion has a significant effect on damage evolution. For the highest applied (maximum) stress of σ_m = 214 MPa, slight strain localization is apparent at the corrosion pit after 5.464 ×10^3 cycles (A_4 in Fig. 6). Two regions IV_1 and IV_2 with high local strain become apparent at 8.078 ×10^3 cycles (B_4 in Fig. 6, indicated by white arrows).These represent two macro-cracks formed at the corrosion pit mouth and sidewall, as clearly shown in the isometric image below; these are associated with point B_4 of the damage curve. With further damage evolution, the dominant macro-crack (IV_1) at the sidewall and the secondary macro-crack IV_2 at the mouth propagated in unstable fashion and coalesce with each other (C_4 in Fig. 6); macro-crack propagation resulted in catastrophe fracture at 8,806 cycles (D_4 in Fig. 6). For $\sigma_m = 187$ MPa, slight strain localization can be found around the corrosion pit at 9,667 cycles, corresponding to A_5 of the damage curve. After 1.645×10^4 cycles, strain concentration region V_1 (B_5 in Fig. 6) occurred at the corrosion pit bottom as shown in the isometric image, reflecting macro-crack V_1 formation. Macro-crack V_1 gradually extends (indicated as C_5 in Fig. 6), eventually resulting in specimen fragmentation failure at 16,672 cycles (D_5 in Fig. 6). Following accumulation of damage for the applied stress of $\sigma_m = 160$ MPa, dominant macro-crack VI_2 was found to nucleate at the corrosion pit sidewall after 2.087×10^4 cycles (B_6 in Fig. 6), and another (secondary) macro-crack VI_1 also formed at the pit mouth, corresponding to point B_6 of the damage curve. Macro-cracks VI_1 and VI_2 continued to propagate with increasing fatigue cycles, coalescing with each other (C_6 in Fig. 6). Ultimately, rapid macro-crack growth resulted in specimen failure at 21,804 cycles (D_6 in Fig. 6).

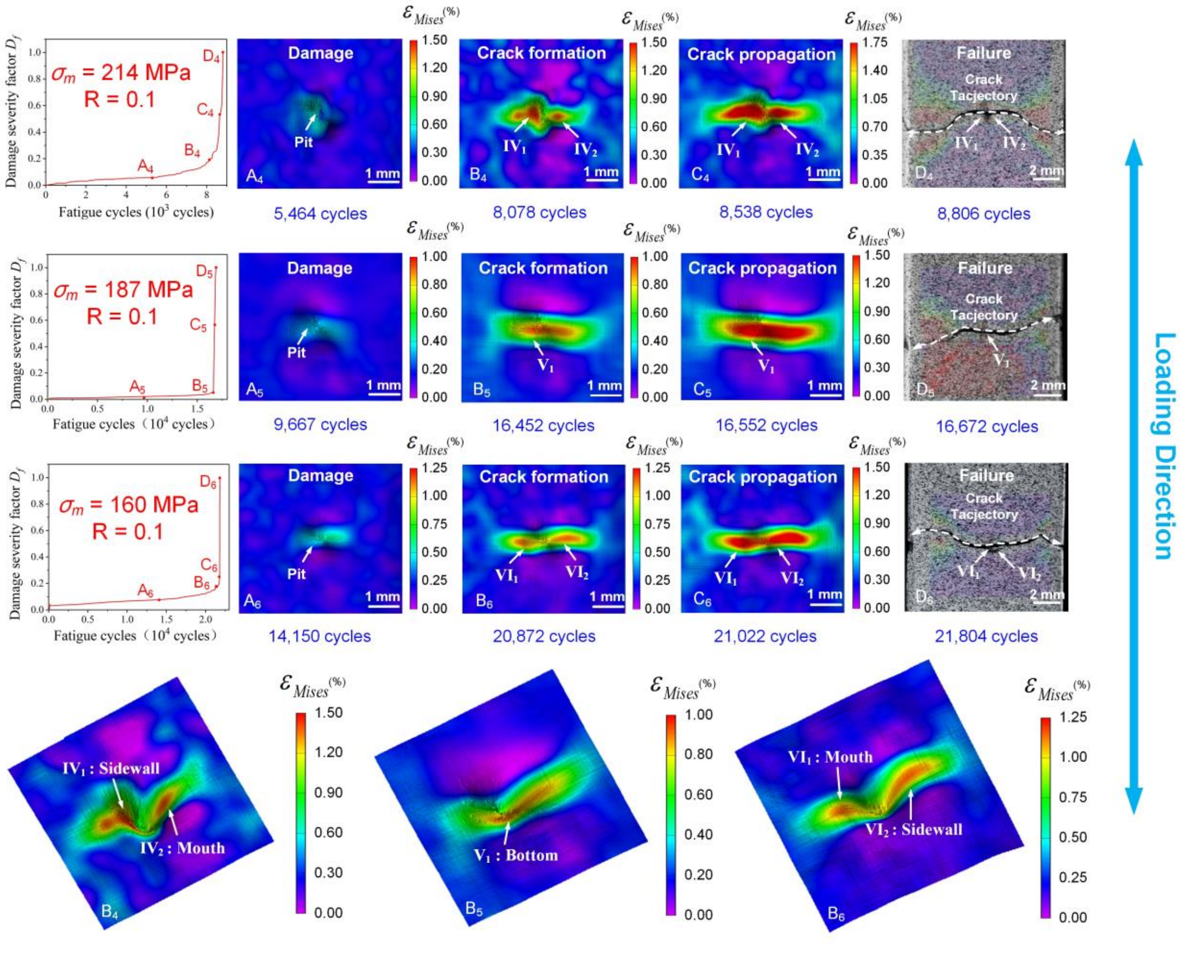

Fig. 6. Visualization of damage evolution, crack formation and propagation in pre-corroded PBF AlSi10Mg specimens under different loading condition, represented by damage severity curves and equivalent strain fields shown in the colored images.

In this section, with the help of 3D-DIC analysis, the spatial and temporal characteristics of fatigue damage evolution, are visualized through the strain field evolution and damage severity curves, focusing on macro-crack formation, propagation and coalescence up to final fracture. A diversity of damage evolution processes and multiple corrosion-induced fatigue macro-cracks were observed; macro-cracking behavior in the critical damage region dominates the failure process.

3.3 Fracture morphology analysis

Based on the 3D-DIC observation, the formation and propagation of macro-cracks is shown to dominate the fatigue failure process. The fracture morphologies of specimens was further observed by SEM, for characterisation of micro-crack nucleation and propagation, combined with DIC-observed macro-crack behavior, for analysis and discussion of the effect of pre-corrosion on fatigue damage and failure.

3.3.1 Crack initiation region

Fig. 7 shows the SEM fracture morphology of the breakthrough crack initiation sites for the uncorroded condition for the three different stress levels (tests) , corresponding to macro-crack initiation areas (I_1 to III_1) identified from the DIC results in Fig. 5. All samples exhibited typical cleavage fracture characteristics. A classic river pattern can be observed at the fracture surface initiation regions, which is generally flat and perpendicular to the nominal load direction. Breakthrough cracks always started from surface/subsurface pores (apparently originating from trapped gas bubbles due to the PBF process) (Fig. 7 a, c, e), which is similar to reports in other AM aluminum alloys[20,22,44-46]. Fig. 7b provides an enlarged view of macro-crack formation zone I_1. The so-called 'kill defect' that promoted micro-crack initiation were LOF pores (represented by un-melted powder particles) on the specimen boundary surface, with a diameter ~105 μm. The micro-cracks propagated and coalesced to form macro-crack I_1, consistent with the DIC observations (Fig. 5, B_1). In the enlarged view of macro-crack II_1 (Fig. 7d) corresponding to Fig. 5 (B_2), it was observed that a cluster of micro-crack initiation sites (yellow arrows) were closely positioned around the un-melted powder pores (diameter ~107 μm). Over time, these micro-cracks underwent progressive growth within the surface and eventually interconnected, giving rise to the formation of ridges. As shown in Fig. 7f, a large number of defects occur inside the PBF specimen, and the unfused pore (diameter ~103 μm) on the surface was still the 'kill defect' leading to fatigue micro-crack initiation. The local stress concentration around the pores caused multiple micro-crack initiation and coalescence to form macro-crack III_1, consistent with the DIC results (Fig. 5, B_3). As cycle numbers increase, these micro-cracks gradually propagated and connected inwards from various directions along the pores, causing ridge features.

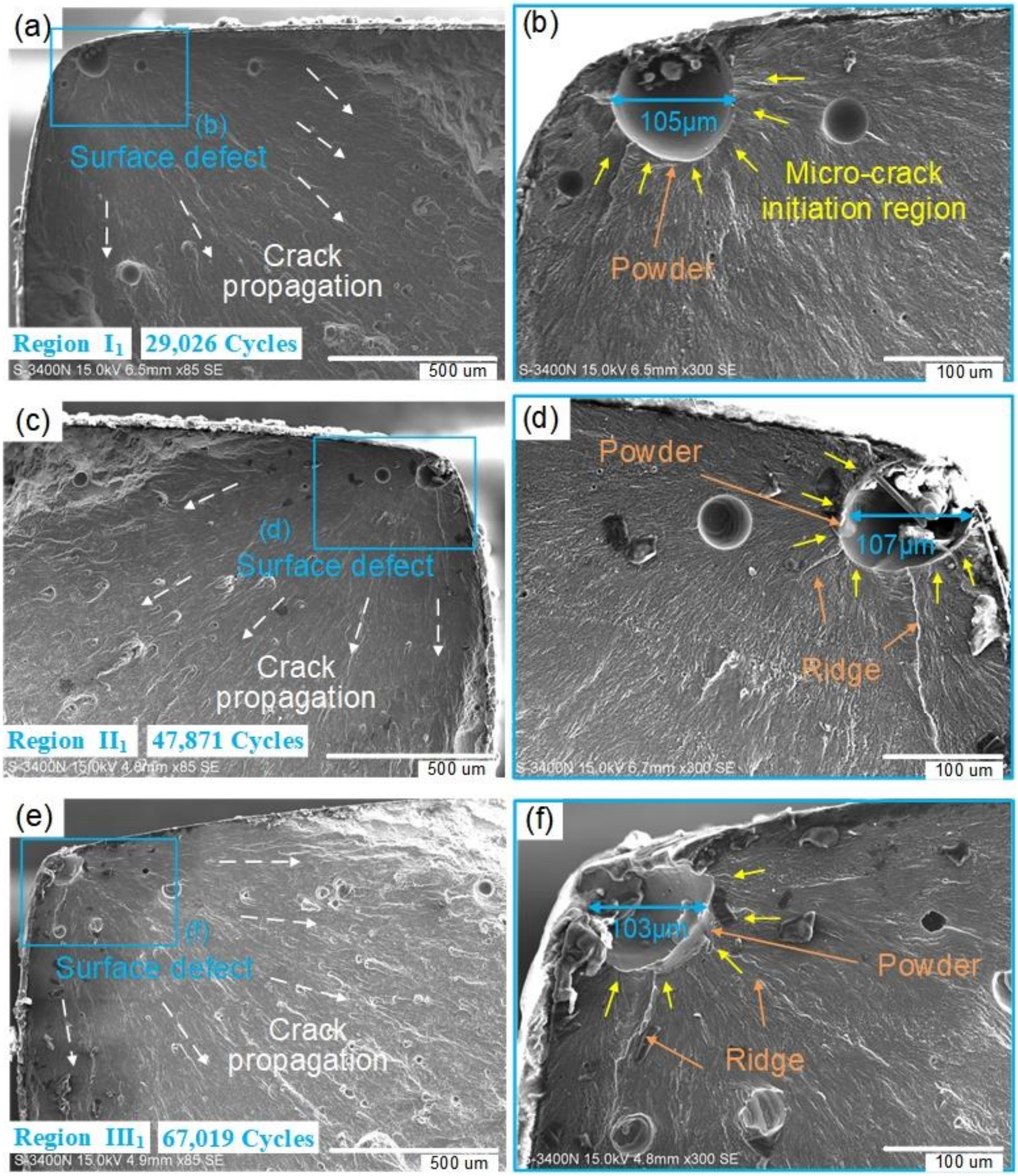

Fig. 7. Typical fracture morphology of uncorroded PBF AlSi10Mg specimen for the three different test applied stress levels; the blue square is the field of view of subsequent images.

According to the 3D-DIC results, the damage evolution of pre-corroded PBF AlSi10Mg under different loading conditions was all caused by central-isolated pits. Further fracture morphology was also analyzed after failure, mainly investigating the micro-crack initiation, propagation and coalescence. Fig. 8 shows the fracture morphologies of three typical pre-corroded specimens at different peak stresses, which corresponded to the regions of macro-crack initiation (IV_1 to VI_2), as identified by the DIC strain fields of Fig. 6. In contrast to the uncorroded condition, the central artificial pre-fabricated corrosion pit served as the origin from which the micro-cracks originated (Fig. 8a, c, e), indicating that the presence of localized corrosion causes stress concentration and promotes micro-crack initiation. The crack propagated radially from the initiation source to the surrounding area. Fig. 8b shows a detailed view of macro-cracks IV_1 and IV_2, where massive micro-crack initiation points were discovered. Numerous micro-cracks initiated and aggregated at the corrosion pit sidewall and bottom (yellow arrows), then continued to propagate, join and gradually evolve into dominant macro-crack IV_1. Multiple micro-cracks nucleate (indicated by green arrows) at the mouth of the corrosion pit, merging to form secondary macro-crack IV_2. The micro-cracks originating from different directions grew and coalesced with each other, causing ridges. As shown in Fig. 8d, substantial micro-cracks originated on the subsurface of the corrosion pit (yellow arrow), appearing to gradually develop and transform into main macro-crack V_1 located at the bottom of the pit (cf. Fig. 6 B_5). On the right side of the corrosion pit, numerous micro-cracks also initiated near the pit mouth, with a distinct cliff-like platform. As shown in the extended visual representations of macro-cracks VI_1 and VI_2 (Fig. 8f), secondary cracks exist within the corrosion pits. On the right side of the pit, multiple micro-cracks nucleated at the mouth, sidewall and bottom (yellow arrows), further propagated, aggregated and gradually evolved into main macro-crack VI_2, with clear fatigue ridge phenomenon. On the left side of the corrosion pit, secondary macro-crack VI_1 also formed via a number of micro-cracks (green arrows) on the sidewall and mouth of the pit. Macro-cracks VI_1 and VI_2 formed on different planes, resulting in obvious cliffs through continuous propagation and coalescence.

In this part, the typical fracture morphologies of the failed specimens were observed by SEM, with specific focus on crack initiation regions, to characterize initiation and early propagation of micro-cracks (corresponding to DIC-identified macro-cracks). The effect of pre-corrosion on fatigue micro-crack initiation is also identified by comparison with the uncorroded case.

3.3.2 Crack propagation and final rupture region

SEM analysis revealed the key mechanisms and phenomena in regions of stable propagation and rupture. As shown in Fig. 9, the fracture surface was uneven, with a disordered distribution of gullies and massive surface defects. The fracture characteristics were similar for the different test load levels and corrosion conditions. For the crack propagation zone shown in Fig. 9a and 9b, a large number of internal defects such as pores, inclusions, and powders determined by the PBF manufacturing process can be seen in various places, which affects the direction of crack propagation. As fatigue cycles increased, a large amount of strain localization around the relevant internal defects can easily lead to secondary crack, as observed elsewhere[18]. The final rupture region exhibited inhomogeneous dimples and typical cleavage fracture features, as shown in Fig. 9c and 9d. Internal defects such as abundant gas-driven pores (based on small size and round shape) and LOF pores (represented by un-melted powder particles), as well as tearing, were also visible in the final rupture region.

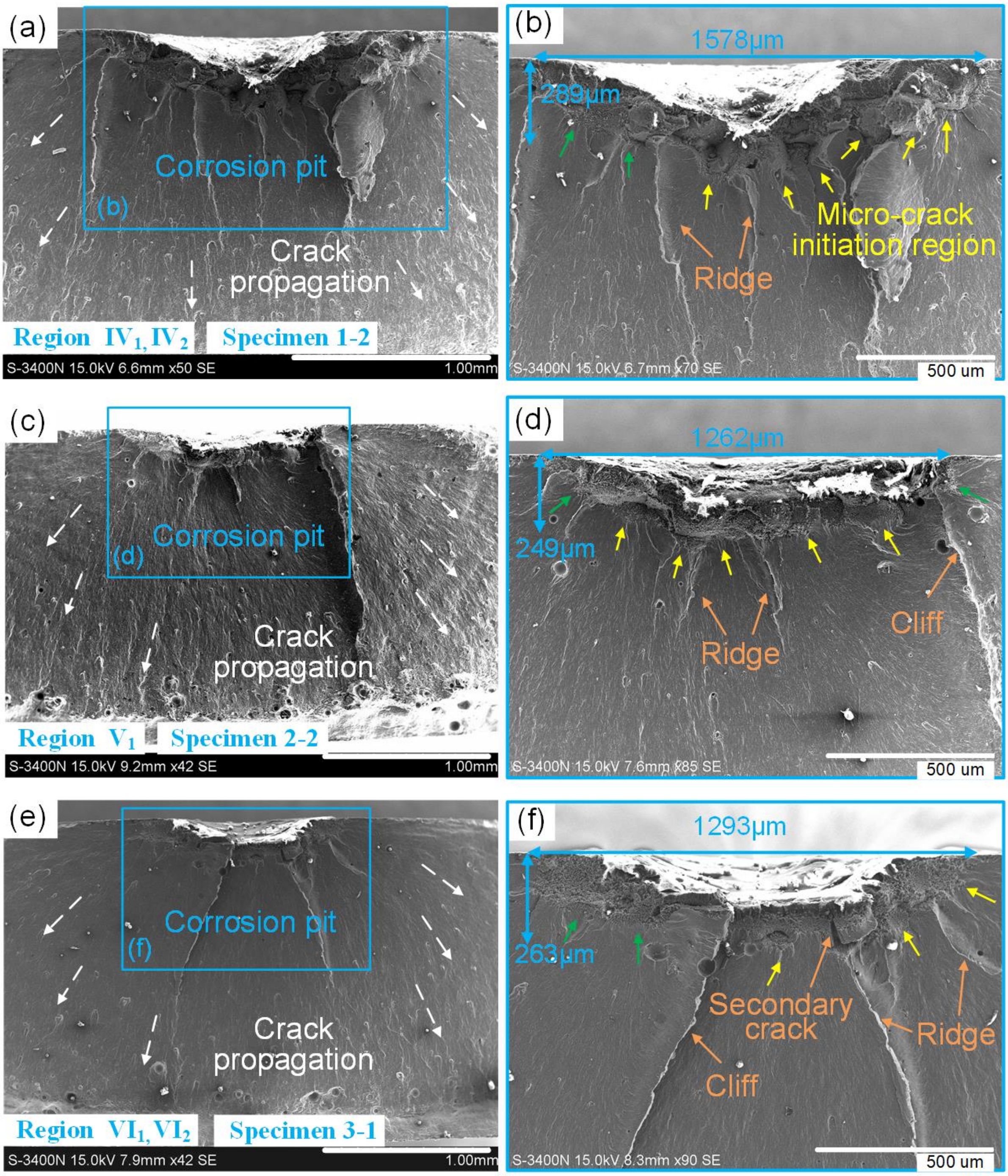

Fig. 8. Typical fracture morphologies of pre-corroded PBF AlSi10Mg specimens under different test (load) conditions; the blue square is the field of view of subsequent images.

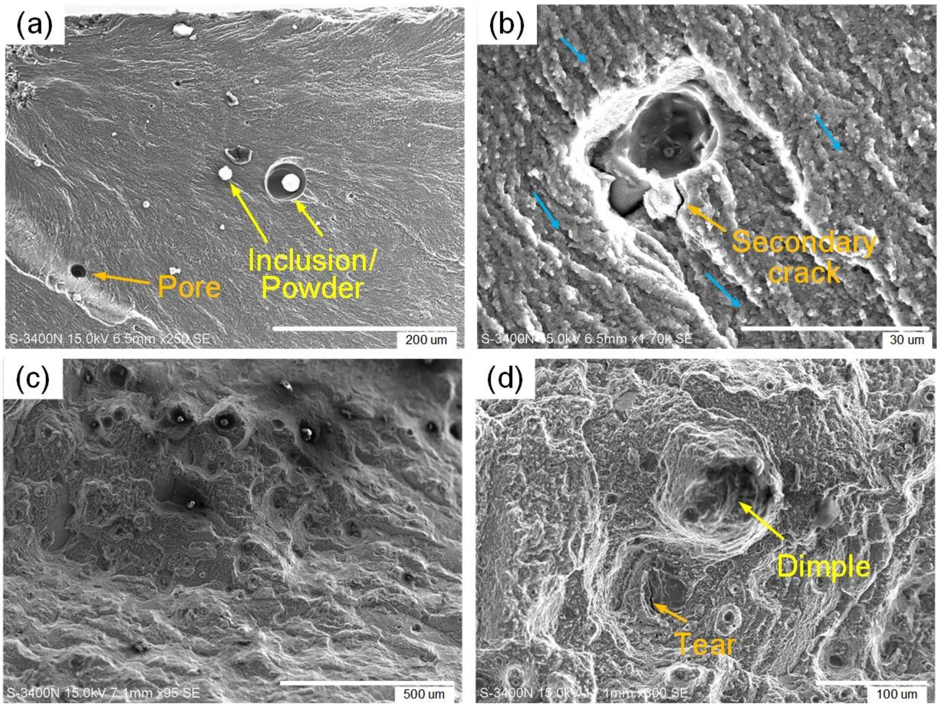

Fig. 9. SEM images of features in crack propagation region and final rupture region.

4. Discussion

4.1 Fatigue damage evolution characteristics

The overall damage evolution process (from macroscopic to microscopic) of PBF aluminum alloy under different fatigue loads and corrosion conditions was qualitatively and quantitatively characterized, via the damage severity curve, DIC-measured evolution of full-field strain distributions, and associated fracture micro-morphologies. For the un-corroded specimens, most of macro-cracks identified by DIC are located at the specimen sidewall, consistent with the SEM fracture analysis. Localized corrosion significantly accelerates the macros-cracks formation under the same loading conditions compared to uncorroded specimens. According to the results obtained from DIC analysis, it can be concluded that the failure process of all pre-corroded specimens is primarily governed by fatigue macro-cracks initiated from the central isolated pit. Multiple corrosion-induced fatigue macro-cracks were observed, and the distinct location (corrosion pit mouth, sidewall, bottom), number and formation time of macro-crack initiation sites are different. As shown in Table 3, most of the macro-cracks identified by DIC initiated at the corrosion pit sidewall or mouth. Two typical failure modes (macro-cracking) are observed: single-crack fracture and multi-crack growth. The single crack mode is more frequently observed in the original (uncorroded) specimens, as shown in Fig. 5 and Fig. 6. Single cracks originate from surface/subsurface defects or localized corrosion and propagate with increasing cycles until failure.

Fig. 6 illustrates the simultaneous growth of multiple cracks in distinct locations within the corrosion pit. The experimental findings demonstrate significant variation in fracture paths across different modes. These fracture modes are dictated by the coupling effect of loading conditions and position of the macro-crack initiation zone, as discussed below further in Section 4.2.

The characteristics of micro-cracks inside the specimens, vis-à-vis the corrosion morphology, were determined by SEM fracture observation. Multiple occurrences of micro-crack initiation was evident in all specimens. For un-corroded conditions, in accordance with the DIC analysis, massive micro-cracks originate from the 'kill defects', internal surface/subsurface LOF pores at the specimen edge (Fig. 7), consistent with previous observations[38,47]. The presence of some small-sized pores in PBF samples is generally tolerated, and optimized PBF process parameters can ensure that most pore sizes are below the threshold for crack initiation. However, the presence of corrosion pits greatly affects the micro-cracking behavior. The SEM (Fig 8) and DIC corroborate the phenomenon of most micro-cracks initiating from pit sidewalls or near-mouth regions, rarely nucleating at the pit bottom. Numerous obvious pores, inclusions and unfused defects can be seen everywhere in the crack propagation zone and forced fracture zone of all specimens (Fig. 9). These internal defects caused by the PBF process affect the crack propagation and speed up PBF part failure.

4.2 Effect of corrosion feature on macro-crack nucleation

To further investigate the effect of corrosion morphology on nucleation of dominant fatigue cracks, the correlation between macro-crack nucleation sites, local corrosion morphology, DIC strain field and SEM fracture morphology was further established. As shown in Fig. 10, combining the 2D top view of fractured corrosion surface under the optical microscope (Fig.10a), the 3D-DIC strain fields determined macro-crack formation location (Fig. 10b), the microscopic fracture shape observed by SEM (Fig. 10c), and the 3D corrosion morphology obtained by the 3D surface measuring instrument (Fig. 10d), the macro-crack nucleation location of each specimen was precisely correlated with the local corrosion morphology and micro-cracking characteristics. According to the 3D-DIC results, the main macro-crack was marked by a yellow rectangle, and the blue rectangle shows secondary macro-cracks not present in every specimen. The extensive characterization and accurate identification of macro-crack initiation features over the entire pre-corroded area enables quantitative assessment of localized corrosion indicators to assess correlation with macro-crack formation. Analyzing this correlation (or lack of) is critical for mechanistically understanding the factors controlling pre-corrosion fatigue crack formation and for identifying key metrics for assessing structural integrity of corrosion components.

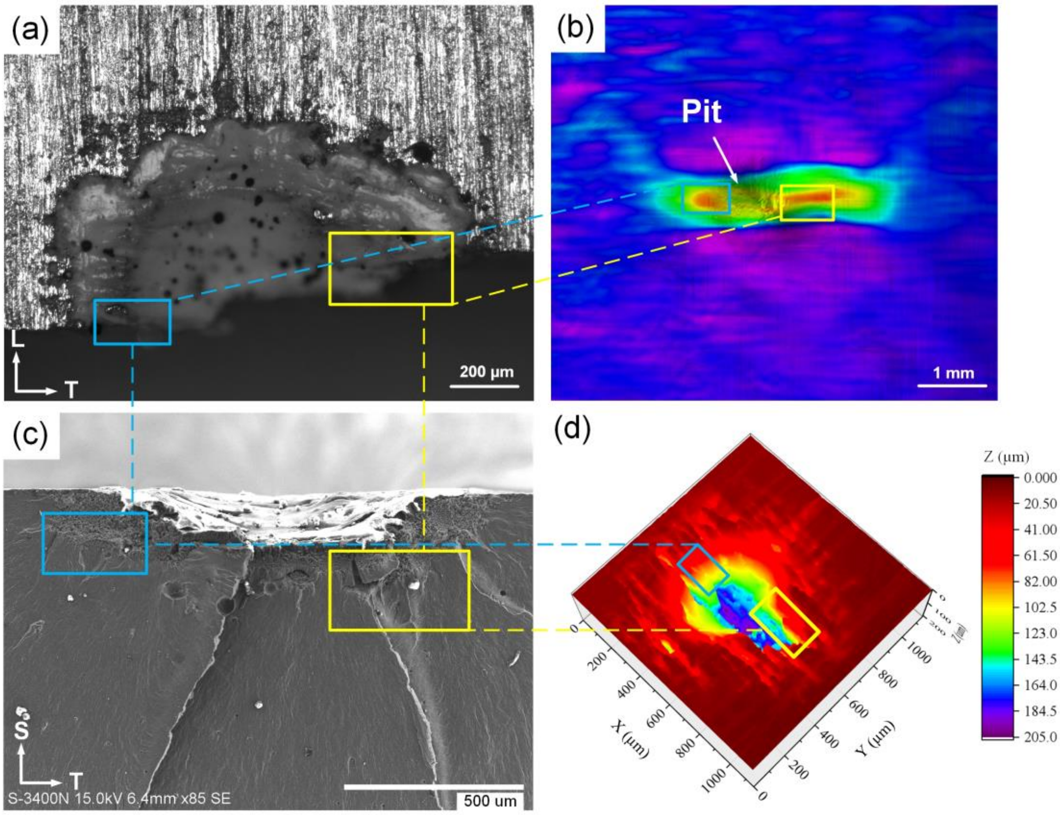

Fig. 10. Correlation between corrosion morphology, DIC strain field and SEM fracture. (a) Fractured corrosion surface (L-T) top view; (b) DIC strain cloud image of macro-crack formation; (c) fracture surface morphology (S-T); (d) 3D morphology of complete corrosion pit. Yellow square represents the main crack initiation locations, and blue square represents the secondary crack initiation locations. Fatigue test of PBF AlSi10Mg, σ_m = 160 MPa, R = 0.1, frequency 5 Hz.

The single corrosion pit in this experiment is a broad surface recession morphology, which is inherently different from more commonly observed (e.g. under in-service conditions) general discrete pitting damage. Therefore, local surface roughness parameters of the corrosion pit are measured to analyze the different indicators inside the corrosion pit. These relevant corrosion features/metrics of fatigue crack initiation locations are obtained from 3D topography measurements analyzed by IFM G5 optical surface measuring instrument. Specifically, each pit surface area is divided into a grid of around 400 µm ×400 µm sections (Fig. 11 (a)), using Alicona software to determine various surface roughness metrics for each mesh section. Here three representative roughness metrics for local regions were taken into consideration: average roughness, root mean square (RMS), and maximum valley depth. Besides, some major fatigue crack initiation locations are plotted on the 3D image of the corrosion pit, as shown in Fig. 11a. The correlation between local corrosion pit topographic characteristics and macro-crack nucleation were analyzed statistically. The histograms of local average roughness, RMS, and maximum valley depth measurements are shown in Fig. 11. For a given specimen, the macro-cracks generally initiate in the area with relatively large values of surface roughness metrics. In addition, Figs. 12a, b, and c shows the relationship between crack initiation position and paired combinations of these roughness metrics for each mesh section. It can be preliminarily found that the region with higher local average roughness and RMS is more likely to form main macro-cracks rather than secondary macro-cracks, although there are still special cases. Other combined results demonstrate a more scattered distribution and no obvious regularity, as shown in Fig. 12b and c: no direct relationship is observed between these metric combinations and the identified macro-crack initiation locations.

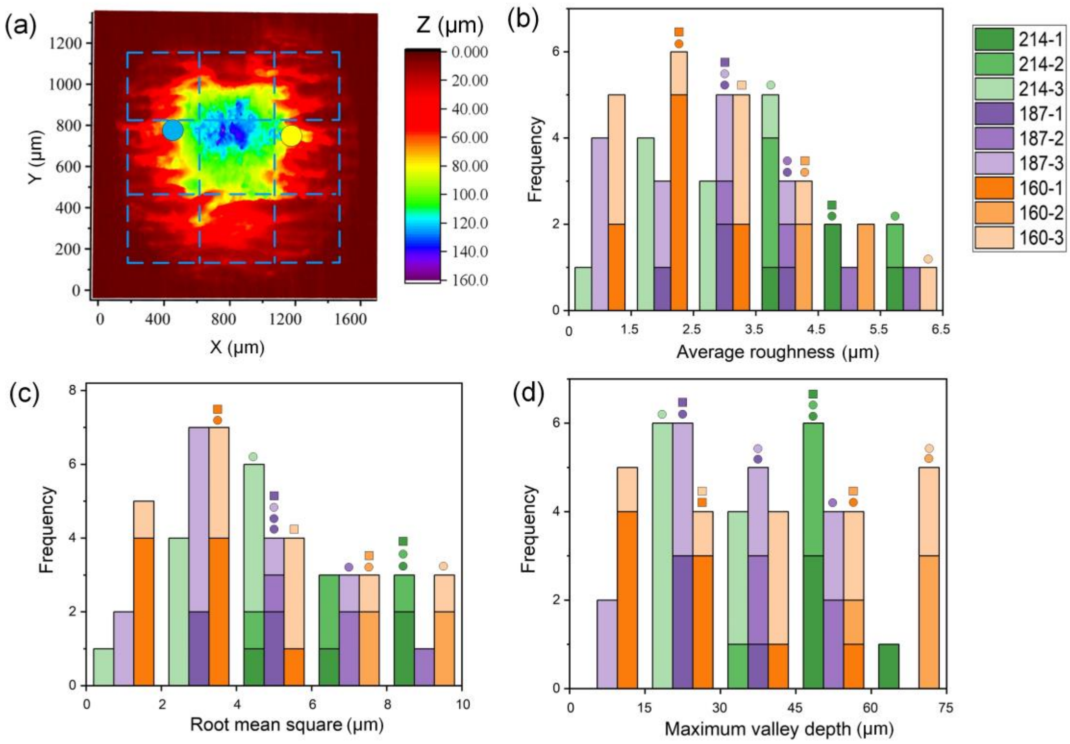

Fig. 11. (a) Top view of 3D corrosion pit morphology, yellow circle represents the main macro-crack initiation locations, and blue circle represents the secondary crack initiation locations; Histograms of (b) average roughness, (c) root mean square (RMS), (d) maximum valley depth; the pitting measurement results of corresponding typical pre-corroded specimens under 214 MPa, 187 MPa and 160 MPa maximum stress are represented by red, blue and green bars. Filled marks indicate the main macro-crack initiation location, while open marks indicate secondary macro-crack initiation sites.

In order to further discuss the influence of peak stress and corrosion pit local morphology on crack initiation position, a random forest machine learning algorithm is used to evaluate feature importance. Random forest is an ensemble learning algorithm based on decision trees as classifiers, which can build multiple decision trees and combine them to produce an overall classification[48-50]. As a result of the population division, the random forest algorithm can predict non-linear or possibly disjointed relationships between variables and responses. In this study, surface roughness representative metrics of central-isolated pits and peak stress were considered as predictor variables. The macro-crack initiation locations identified by DIC in each specimen were assigned a response value of 1, and all other data sites not corresponding to a specific formation location were assigned a response value of 0. There are three repeated experiments under different peak stresses; two of these were used for parameter training and the third for test evaluation to construct a random forest model. The model combined large numbers of these partitions or decision trees and votes to predict probability of generating macro-cracks. The resulting relative importance of average roughness, RMS, maximum valley depth in local region, and peak stress for crack initiation location were: 0.45, 0.29, 0.19, 0.07, respectively. As shown in Fig. 12d, the comprehensive feature importance ranking shows that local average roughness has the greatest effect on prediction of the initiation position. Crucially, the corrosion pit surface local region features are primarily investigated here, the analysis of the crack initiation location in the context of the corroded region shape appears to be beneficial. Based on the above discussion, it can be deduced that corrosion surface roughness is a key parameter for crack initiation position, i.e. macro-cracks are more likely to appear in regions of larger corrosion surface roughness. For individual exceptions to these results, it is believed that the interactions between corrosion micro-features, material defects, and material microstructure inside local regions can also accelerate crack initiation[51].

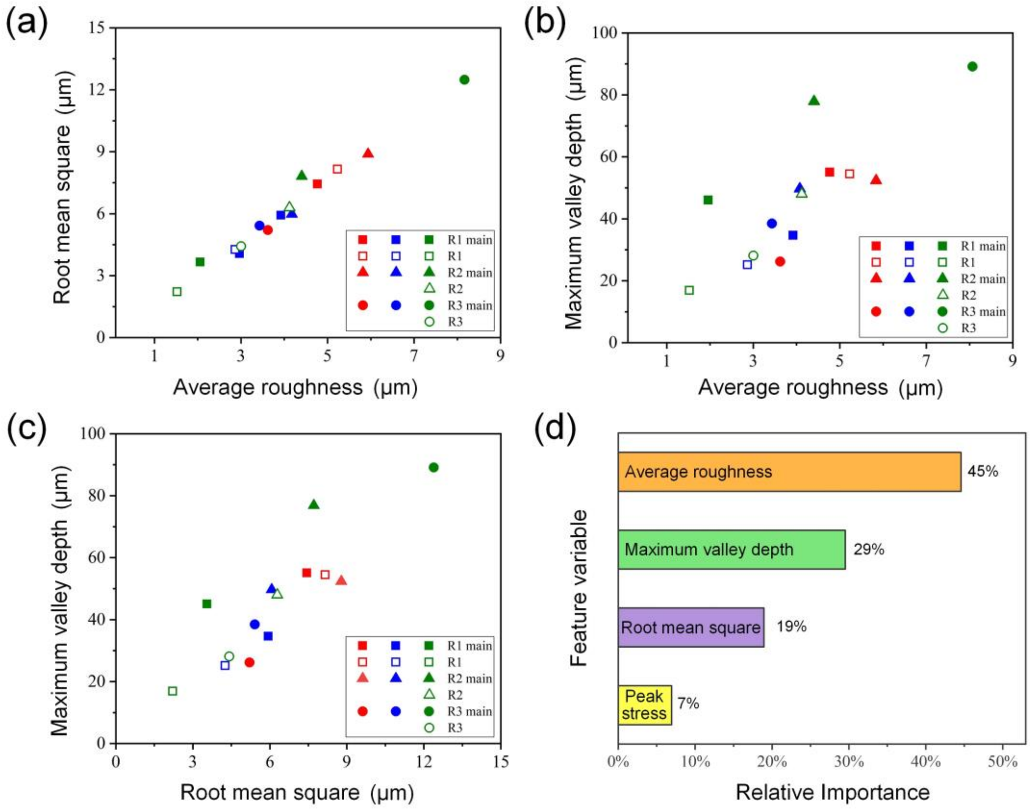

Fig. 12. Plot of the combination effects on (a) RMS and average roughness; (b) maximum valley depth and average roughness; (c) maximum valley depth and RMS for pre-corroded specimens. Three different loading conditions (σ_m =214 MPa, 187 MPa, 160 MPa) are distinguished by red, blue and green, respectively. Filled marks indicate the main macro-crack initiation location, while open marks indicate secondary macro-crack initiation sites. R1, R2, R3 correspond to three test replicates. (d) Relative importance of roughness metrics and peak stress.

4.3 Micro-crack initiation mechanism

Un-melted particles and pore defects on the surface/subsurface can cause stress concentrations and lead to crack initiation. As discussed by Wang *et al.*, the pores generated during the PBF process and the weak interfacial debonding between the particles and the α-Al matrix are likely to be the main reasons for porosity defect formation[52]. The stress concentration near the defect produces small cleavage cracks, and with continuous external loading, the surrounding matrix undergoes plastic failure, which promotes crack initiation and propagation[53]. In order to further explore the uniaxial fatigue micro-crack initiation mechanism of pre-corroded PBF AlSi10Mg, a total of 84 micro-cracks were identified and classified according to the SEM fractography. As shown in Fig. 13, four typical micro-crack initiation forms were identified: internal defect, corrosion platform, corrosion micro-pit, and corrosion jut, in which the micro-crack initiation forms of internal defect and corrosion platform are unique features for PBF AlSi10Mg compared with traditional aluminum alloy[54]. Regarding the mechanism analysis of internal defects causing micro-crack initiation, the micro-scale stress concentration caused by the surrounding microstructural defects like inclusions, pores, un-melted particles may jointly enhance the driving force for micro-crack initiation[31,36]. Interestingly, a relatively flat rough corrosion morphology, continuously along the corrosion surface, was usually found at the mouth and bottom of the corrosion pit, mainly composed of shallow corrosion pit and clusters; this was classified as a corrosion platform with rough surface. It can be considered that such shallow corrosion features tend to induce microscale plastic strain concentrations near the corrosion damage. There is also a view that the presence of such high surface roughness is more likely to act as sites for intergranular corrosion[55,56]. Combined with AM material microstructural properties, when the load is perpendicular to the build direction, the grain boundaries along the interior of the material are more likely to cause slip dislocation accumulation. When the load is perpendicular to the forming direction, slip dislocations are more likely to accumulate along the columnar grain boundaries aligned parallel to the build direction[57]. These increasing corrosion-induced stresses and strains interact with susceptible microstructural features surrounding the corrosion damage, prompting formation of numerous micro-cracks almost immediately[36]. Some other obvious corrosion micro-features (corrosion micro-pit, corrosion jut) are also distributed around the corrosion pits. Corrosion micro-pits are about 30 to 50 μm deep. Corrosion juts (protruding from the metal volume) are metal protrusions between 30 and 40 μm in length along the corroded surface. Such corrosion micro-features can cause localized stress-strain concentrations to promote crack formation[54,58]. Burns *et al.* demonstrated that the presence of these kinds of micro features increased $k_{t\text{-}e}$ and k_{ε} by an average of 115% and 175% based on finite element analysis of traditional aluminum alloy 7050-T7451[36].

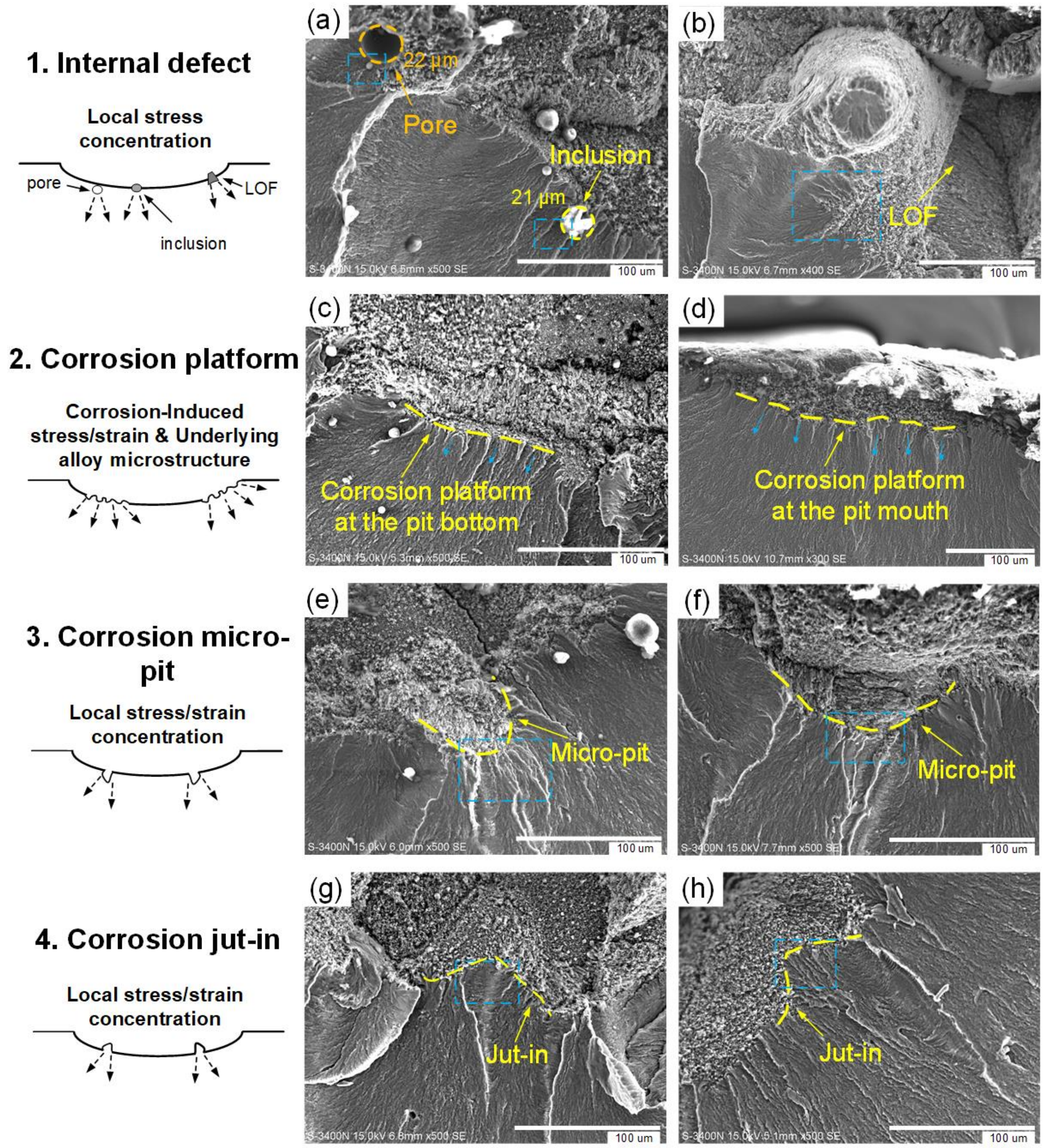

Fig. 13. Four micro-crack initiation forms of pre-corroded PBF AlSi10Mg specimens under uniaxial fatigue: 1. Internal defect, 2. Corrosion platform, 3. Corrosion micro-pit, 4. Corrosion jut-in; (a-h) are the corresponding SEM fracture morphologies, respectively, the micro-crack initiation site is indicated in blue dotted box.

The statistical histograms of fatigue micro-crack initiation forms for PBF AlSi10Mg with central isolated corrosion pit under uniaxial fatigue loading are shown in Fig. 14; cases which do not fall into the latter four general types are in the category "others". Relative to other peak stress values, the number of initiation sites under low load increased significantly. The above four general types (internal defects, corrosion platform, corrosion micro-pit, and corrosion jut) account for 17%, 17%, 37%, and 23%, respectively. Corrosion micro-features (micro-pit and jut) are common fatigue micro-crack initiation mechanisms[59], and micro-pits, as the most common nucleating feature, have been confirmed by relevant finite element analysis to have a higher localized strain level than juts[36]. In general, the typical corrosion micro-features (corrosion micro-pit, corrosion jut-in and corrosion platform) produced by pre-corrosion have a large impact on micro-crack initiation, only a few occur at self-defects due to material manufacturing. However, combined with the fracture morphology of the corrosion pits, there are still multiple associated micro-crack initiation points around the corrosion micro-features with the highest frequency. The higher the number of localized corrosion micro-features, the higher the probability that their interaction with the microstructure inside the material will induce further micro-crack initiation. In other words, fatigue micro-crack initiation in pre-corroded PBF aluminum alloys is not controlled further by either corrosion morphology or material underlying structure, but is more likely to be a coupling effect of corrosion macro/micro morphology, underlying microstructure, internal defects and loading conditions. Further research is needed to examine the effect of coupled control of localized corrosion micro-features and nearby underlying alloy microstructure on crack initiation.

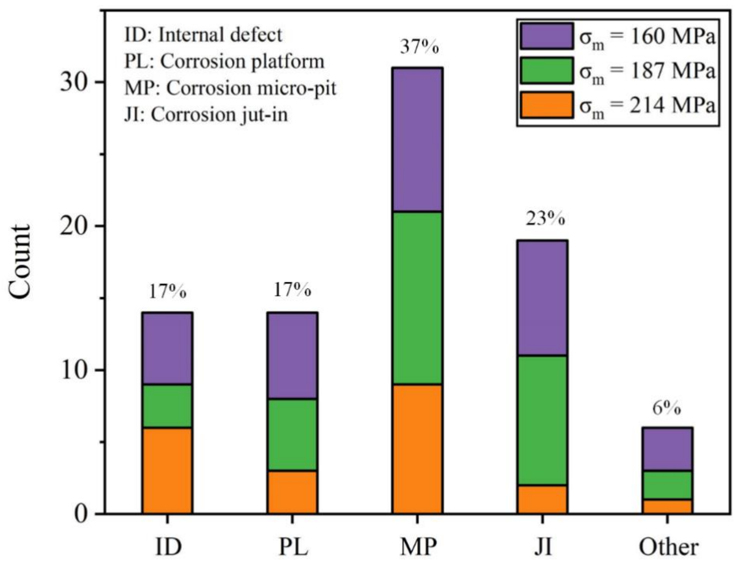

Fig. 14. Histogram of the micro-crack initiation forms for PBF AlSi10Mg specimens with central corrosion pit under uniaxial loading (binned based on the types such as internal defect, corrosion platform, corrosion micro-pit, corrosion jut-in). The initiation forms that do not fit in the classification are binned as others.

5. Conclusions

This paper presents a micro-macro scale experimental investigation on the effect of pre-corrosion on fatigue damage evolution and crack initiation mechanisms for PBF AlSi10Mg using a methodology comprising a combination of 3D corrosion topography measurement, 3D DIC, SEM characterization, and data-science analysis. The main conclusions are as follows:

(1) An experimental strategy was proposed to provide multi-source experimental information of 3D corrosion morphology, DIC strain field evolution, and SEM fracture morphology, which can effectively characterize the damage evolution of pre-corroded PBF aluminum alloy.

(2) Macro-scale cracks initiated in the sidewall and mouth of the corrosion pit, and a few cracks originated from the bottom region. Two typical failure modes were observed: single-crack fracture and multi-crack growth, which are determined by the coupling effects of loading conditions and macro-crack initiation zone.

(3) Through statistical analysis of the surface roughness metrics in local regions (average roughness, RMS, maximum valley depth), it is found that macroscopic cracks are more likely to initiate in local areas with large corrosion surface roughness. The relative importance of representative roughness metrics and peak stress affecting the initiation location was ranked based on a random forest model: average roughness > RMS > maximum valley depth > peak stress.

(4) For un-corroded conditions, micro-cracking mostly originated from surface/subsurface LOF defects. For pre-corroded specimens, four typical fatigue micro-crack initiation types were observed, namely internal defects (inclusions, pores, un-melted particles), corrosion platform, corrosion micro-pit and corrosion juts. Internal defects and corrosion platform are characteristic features for PBF AlSi10Mg compared with traditional aluminum alloy. Statistical analysis shows that corrosion micro-pit and corrosion juts accounted for the majority of the micro-crack initiation forms (37% and 23%, respectively).

(5) The micro-crack initiation mechanism for the four main types (internal defects, corrosion platform, corrosion micro-pit and corrosion juts) is a combination of local stress concentration due to nearby material micro-structural defects, interaction of underlying alloy microstructure and corrosion-induced stress-strain state, and local stress-strain concentration at corrosion micro-features.

Data Availability Statement

The raw/processed data required to reproduce these findings cannot be shared at this time as the data also forms part of an ongoing study.

Acknowledgements

For the purpose of Open Access, the author has applied a CC BY public copyright licence to any Author Accepted Manuscript version arising from this submission. This research was supported by the National Natural Science Foundation of China (NSFC, Grant Nos. 12372188 and 11972364), the Fundamental Research Funds for the

Central Universities (FRFCU, Grant No. 3122022102). SBL is funded by Science Foundation Ireland under grant numbers SFI 22/FFP-A/10299 and SFI 21/RC/10295_P2.

References

[1] Wu Z, Wu S, Qian W, Zhang H, Zhu H, et al. Structural integrity issues of additively manufactured railway components: Progress and challenges. *Engineering Failure Analysis.* 2023;149:107265.

[2] Wischeropp TM, Emmelmann C, Brandt M, Pateras A. Measurement of actual powder layer height and packing density in a single layer in selective laser melting. *Additive Manufacturing.* 2019;28:176-183.

[3] Olakanmi EO, Cochrane RF, Dalgarno KW. A review on selective laser sintering/melting (SLS/SLM) of aluminium alloy powders: Processing, microstructure, and properties. *Progress in Materials Science.* 2015;74:401-477.

[4] Leuders S, Thöne M, Riemer A, Niendorf T, Tröster T, et al. On the mechanical behaviour of titanium alloy TiAl6V4 manufactured by selective laser melting: Fatigue resistance and crack growth performance. *International Journal of Fatigue.* 2013;48:300-307.

[5] Zhang Y, Li X, Yuan S, Sun R, Sakai T, et al. High-cycle-fatigue properties of selective-laser-melted AlSi10Mg with multiple building directions. *International Journal of Mechanical Sciences.* 2022;224:107336.

[6] Fathi P, Mohammadi M, Duan X, Nasiri AM. A comparative study on corrosion and microstructure of direct metal laser sintered AlSi10Mg_200C and die cast A360.1 aluminum. *Journal of Materials Processing Technology.* 2018;259:1-14.

[7] Bi J, Lei Z, Chen Y, Chen X, Lu N, et al. An additively manufactured Al-14.1Mg-0.47Si-0.31Sc-0.17Zr alloy with high specific strength, good thermal stability and excellent corrosion resistance. *Journal of Materials Science & Technology.* 2021;67:23-35.

[8] Sander G, Birbilis N, Tan J, Balan P, Gharbi O, et al. Corrosion of Additively Manufactured Alloys: A Review. *Corrosion -Houston Tx-.* 2018;74.

[9] Torbati-Sarraf H, Torbati-Sarraf SA, Chawla N, Poursaee A. A comparative study of corrosion behavior of an additively manufactured Al-6061 RAM2 with extruded Al-6061 T6. *Corrosion Science.* 2020;174.

[10] Zhang X, Lv Y, Tan S, Dong Z, Zhou X. Microstructure and corrosion behaviour of wire arc additive manufactured AA2024 alloy thin wall structure. *Corrosion Science.* 2021;186:109453.

[11] Marina C, Flaviana C, Paolo F, Sergio L, Massimo L, et al. Corrosion Behavior of Heat-Treated AlSi10Mg Manufactured by Laser Powder Bed Fusion. *Materials.* 2018;11(7):1051-.

[12] Zakay A, Aghion E. Effect of Post-heat Treatment on the Corrosion Behavior of AlSi10Mg Alloy Produced by Additive Manufacturing. *Jom.* 2019;71(3):1150-1157.

[13] Cabrini M, Lorenzi S, Pastore T, Pellegrini S, Ambrosio EP, et al. Effect of heat treatment on corrosion resistance of DMLS AlSi10Mg alloy. *Electrochimica Acta.* 2016;206:346-355.

[14] Leon A, Aghion E. Effect of surface roughness on corrosion fatigue performance of AlSi10Mg alloy produced by Selective Laser Melting (SLM). *Materials Characterization.* 2017;131:188-194.

[15] Girelli L, Tocci M, Conte M, Giovanardi R, Veronesi P, et al. Effect of the T6 heat treatment on corrosion behavior of additive manufactured and gravity cast AlSi10Mg alloy. *Materials and Corrosion.* 2019;70(10):1808-1816.

[16] Wei P, Chen Z, Zhang S, Fang X, Lu B, et al. Effect of T6 heat treatment on the surface tribological and corrosion properties of AlSi10Mg samples produced by selective laser melting. *Materials Characterization.* 2021;171.

[17] Rubben T, Revilla RI, De Graeve I. Influence of heat treatments on the corrosion mechanism of additive manufactured AlSi10Mg. *Corrosion Science.* 2019;147:406-415.

[18] GlodeŽ S, Klemenc J, ZupaniČ F, Vesenjak M. High-cycle fatigue and fracture behaviours of SLM AlSi10Mg alloy. *Transactions of Nonferrous Metals Society of China.* 2020;30(10):2577-2589.

[19] Romano S, Patriarca L, Foletti S, Beretta S. LCF behaviour and a comprehensive life prediction model for

AlSi10Mg obtained by SLM. *International Journal of Fatigue.* 2018;117:47-62.

[20] Beretta S, Romano S. A comparison of fatigue strength sensitivity to defects for materials manufactured by AM or traditional processes. *International Journal of Fatigue.* 2017;94:178-191.

[21] Niu X, Zhu S-P, He J-C, Liao D, Correia JAFO, et al. Defect tolerant fatigue assessment of AM materials: Size effect and probabilistic prospects. *International Journal of Fatigue.* 2022;160:106884.

[22] Ferro P, Fabrizi A, Berto F, Savio G, Meneghello R, et al. Defects as a root cause of fatigue weakening of additively manufactured AlSi10Mg components. *Theoretical and Applied Fracture Mechanics.* 2020;108.

[23] Niu X, Zhu S-P, He J-C, Luo C, Wang Q. Probabilistic and defect tolerant fatigue assessment of AM materials under size effect. *Engineering Fracture Mechanics.* 2023;277:109000.

[24] Wang L, Zhu S-P, Luo C, Niu X, He J-C. Defect driven physics-informed neural network framework for fatigue life prediction of additively manufactured materials. 2023;381(2260):20220386.

[25] Aboulkhair NT, Simonelli M, Parry L, Ashcroft I, Tuck C, et al. 3D printing of Aluminium alloys: Additive Manufacturing of Aluminium alloys using selective laser melting. *Progress in Materials Science.* 2019;106.

[26] Gorsse S, Hutchinson C, Goune M, Banerjee R. Additive manufacturing of metals: a brief review of the characteristic microstructures and properties of steels, Ti-6Al-4V and high-entropy alloys. *Sci Technol Adv Mater.* 2017;18(1):584-610.

[27] Seede R, Shoukr D, Zhang B, Whitt A, Gibbons S, et al. An ultra-high strength martensitic steel fabricated using selective laser melting additive manufacturing: Densification, microstructure, and mechanical properties. *Acta Materialia.* 2020;186:199-214.

[28] Wang Z, Wu W, Qian G, Sun L, Li X, et al. In-situ SEM investigation on fatigue behaviors of additive manufactured Al-Si10-Mg alloy at elevated temperature. *Engineering Fracture Mechanics.* 2019;214:149-163.

[29] Larrosa NO, Wang W, Read N, Loretto MH, Evans C, et al. Linking microstructure and processing defects to mechanical properties of selectively laser melted AlSi10Mg alloy. *Theoretical and Applied Fracture Mechanics.* 2018;98:123-133.

[30] Wu Z, Wu S, Bao J, Qian W, Karabal S, et al. The effect of defect population on the anisotropic fatigue resistance of AlSi10Mg alloy fabricated by laser powder bed fusion. *International Journal of Fatigue.* 2021;151:106317.

[31] Jian ZM, Qian GA, Paolino DS, Tridello A, Berto F, et al. Crack initiation behavior and fatigue performance up to very-high-cycle regime of AlSi10Mg fabricated by selective laser melting with two powder sizes. *International Journal of Fatigue.* 2021;143:106013.

[32] Brandl E, Heckenberger U, Holzinger V, Buchbinder D. Additive manufactured AlSi10Mg samples using Selective Laser Melting (SLM): Microstructure, high cycle fatigue, and fracture behavior. *Materials & Design.* 2012;34:159-169.

[33] Uzan NE, Ramati S, Shneck R, Frage N, Yeheskel O. On the effect of shot-peening on fatigue resistance of AlSi10Mg specimens fabricated by additive manufacturing using selective laser melting (AM-SLM). *Additive Manufacturing.* 2018;21:458-464.

[34] Bagherifard S, Beretta N, Monti S, Riccio M, Bandini M, et al. On the fatigue strength enhancement of additive manufactured AlSi10Mg parts by mechanical and thermal post-processing. *Materials & Design.* 2018;145:28-41.

[35] Aboulkhair NT, Maskery I, Tuck C, Ashcroft I, Everitt NM. Improving the fatigue behaviour of a selectively laser melted aluminium alloy: Influence of heat treatment and surface quality. *Materials & Design.* 2016;104:174-182.

[36] Burns JT, Larsen JM, Gangloff RP. Driving forces for localized corrosion-to-fatigue crack transition in Al–Zn–Mg–Cu. *Fatigue & Fracture of Engineering Materials & Structures.* 2011;34(10):745-773.

[37] Arunachalam S, Fawaz S. Test method for corrosion pit-to-fatigue crack transition from a corner of hole in 7075-T651 aluminum alloy. *International Journal of Fatigue.* 2016;91:50-58.
[38] Qian G, Jian Z, Qian Y, Pan X, Ma X, et al. Very-high-cycle fatigue behavior of AlSi10Mg manufactured by selective laser melting: Effect of build orientation and mean stress. *International Journal of Fatigue.* 2020;138:105696.
[39] Singh AK, Datta S, Chattopadhyay A, Riddick JC, Hall AJ. Fatigue crack initiation and propagation behavior in Al – 7075 alloy under in-phase bending-torsion loading. *International Journal of Fatigue.* 2019;126:346-356.
[40] Standard Test Method for Exfoliation Corrosion Susceptibility in 2XXX and 7XXX Series Aluminum Alloys (EXCO Test). *Astm.*
[41] Alexopoulos ND, Migklis E, Stylianos A, Myriounis DP. Fatigue behavior of the aeronautical Al–Li (2198) aluminum alloy under constant amplitude loading. *International Journal of Fatigue.* 2013;56:95-105.
[42] Song H, Liu C, Zhang H, Yang X, Chen Y, et al. Experimental investigation on damage evolution in pre-corroded aluminum alloy 7075-T7651 under fatigue loading. *Materials Science and Engineering: A.* 2021;799.
[43] OH B. The exponential law of endurance tests. Paper presented at: Proc Am Soc Test Mater1910.
[44] Qian W, Wu S, Wu Z, Ahmed S, Zhang W, et al. In situ X-ray imaging of fatigue crack growth from multiple defects in additively manufactured AlSi10Mg alloy. *International Journal of Fatigue.* 2022;155:106616.
[45] Chen J, Hou W, Wang X, Chu S, Yang Z. Microstructure, porosity and mechanical properties of selective laser melted AlSi10Mg. *Chinese Journal of Aeronautics.* 2020;33(7):2043-2054.
[46] Wang P, Deng L, Prashanth KG, Pauly S, Eckert J, et al. Microstructure and mechanical properties of Al-Cu alloys fabricated by selective laser melting of powder mixtures. *Journal of Alloys and Compounds.* 2018;735:2263-2266.
[47] Song H, Sun L, Du J. Effect of Pre-corrosion on the Fatigue Failure of Additive Manufactured AlSi10Mg Alloy. *Journal of Materials Engineering and Performance.* 2021.
[48] Kusano M, Miyazaki S, Watanabe M, Kishimoto S, Bulgarevich DS, et al. Tensile properties prediction by multiple linear regression analysis for selective laser melted and post heat-treated Ti-6Al-4V with microstructural quantification. *Materials Science and Engineering: A.* 2020;787:139549.
[49] Thakur D, Biswas S. An Integration of feature extraction and Guided Regularized Random Forest feature selection for Smartphone based Human Activity Recognition. *Journal of Network and Computer Applications.* 2022;204:103417.
[50] Zhao Y, Zhu W, Wei P, Fang P, Zhang X, et al. Classification of Zambian grasslands using random forest feature importance selection during the optimal phenological period. *Ecological Indicators.* 2022;135:108529.
[51] Cerit M, Genel K, Eksi S. Numerical investigation on stress concentration of corrosion pit. *Engineering Failure Analysis.* 2009;16(7):2467-2472.
[52] Wang Y, Liu Z, Zhou Y, Yang X, Tang J, et al. Microstructure and mechanical properties of TiN particles strengthened 316L steel prepared by laser melting deposition process. *Materials Science and Engineering: A.* 2021;814:141220.
[53] Feng Z, Tan H, Fang Y, Lin X, Huang W. Selective laser melting of TiB2/AlSi10Mg composite: Processability, microstructure and fracture behavior. *Journal of Materials Processing Technology.* 2022;299:117386.
[54] Co NEC, Burns JT. Effects of micro-scale corrosion damage features and local microstructure on fatigue crack initiation location. *International Journal of Fatigue.* 2021;150:106301.
[55] Mohammadi M, Asgari H. Achieving low surface roughness AlSi10Mg_200C parts using direct metal laser sintering. *Additive Manufacturing.* 2018;20:23-32.

[56] Zou Y, Liu Q, Jia Z, Xing Y, Ding L, et al. The intergranular corrosion behavior of 6000-series alloys with different Mg/Si and Cu content. *Applied Surface Science.* 2017;405:489-496.

[57] Kok Y, Tan XP, Wang P, Nai MLS, Loh NH, et al. Anisotropy and heterogeneity of microstructure and mechanical properties in metal additive manufacturing: A critical review. *Materials & Design.* 2018;139:565-586.

[58] van der Walde K, Hillberry BM. Initiation and shape development of corrosion-nucleated fatigue cracking. *International Journal of Fatigue.* 2007;29(7):1269-1281.

[59] Burns JT, Kim S, Gangloff RP. Effect of corrosion severity on fatigue evolution in Al–Zn–Mg–Cu. *Corrosion Science.* 2010;52(2):498-508.